Excellent high-pressure-sustainable thermoelectric performance driven by metal-insulator topological phase transition in semimetal CaCdGe

Liangyu Li,[1,2] Zhenyu Ding,[1,2] Rongman Gao,[1,2] Miao Li,[1,2] Shuo-Wang Yang,[3] Gang Wu[3,*] and Xiaoping Yang[1,†]

[1]*High Magnetic Field Laboratory of Anhui Province, High Magnetic Field Laboratory, HFIPS, Chinese Academy of Sciences, Hefei 230031, China*

[2]*Science Island Branch of Graduate School, University of Science and Technology of China, Hefei 230026, China*

[3]*Materials Science and Chemistry, Institute of High Performance Computing (IHPC), Agency for Science, Technology and Research (A*STAR), 1 Fusionopolis Way, #16-16 Connexis, Singapore 138632, Republic of Singapore*

Recent advances in thermoelectric research have shed light on the promising properties of topological semimetals, which exhibit superior carrier mobility and electrical conductivity compared to traditional thermoelectric materials. Herein, we employ a first-principles method and semiclassical Boltzmann transport theory to investigate the electronic structures, lattice dynamics, and thermoelectric performance of CaCdGe, a representative nodal-line semimetal, along with their response to pressure. Our findings reveal that CaCdGe possesses an ultralow lattice thermal conductivity at room temperature (0.765 $Wm^{-1}K^{-1}$) and exhibits excellent n-type thermoelectric behavior in a wide temperature range. Specifically, we identify in-plane (out-of-plane) maximum thermoelectric figures of merit, ZT_{max}, reaching 1.02 (0.65) at 700 K(1100 K). Remarkably, even under extreme conditions of high pressure (up to 50 GPa), CaCdGe maintains its structural stability without undergoing any structural phase transition. Moreover, we explore the impact of spin-orbit coupling and observe a pressure-driven Lifshitz transition of the Fermi surface around 40 GPa. This transition results in CaCdGe undergoing an electronic phase transition from a charge-compensated semimetal to a topological insulator. Intriguingly, the thermoelectric parameters exhibit unconventional pressure response, embodied by the insensitivity to high pressure after electronic phase transition. Notably, even at 50 GPa, the in-plane (out-of-plane) ZT_{max} reaches 1.2 (0.7) at 1500 K(500 K). Our comprehensive theoretical study demonstrates the immense potential of CaCdGe and related topological semimetals for thermoelectric applications, even in extreme conditions of high pressure and high temperature.

I. INTRODUCTION

Thermoelectric materials hold great promise for converting waste heat into electrical energy, thereby enhancing energy consumption efficiency for a sustainable future. They can be fabricated into power generation devices with outstanding advantages such as ecofriendliness, precise temperature control, suitability for extreme conditions, robustness, durability, and silent operation. While inorganic thermoelectric research has traditionally focused on semiconductors with intermediate band gaps, recent attention has shifted toward topological semimetals [1–6]. These materials, characterized by robust linear crossing bands and associated topological boundary states [7–11], exhibit larger carrier mobility and electrical conductivity [12,13]. Moreover, they often consist of heavy elements with strong spin-orbit coupling (SOC), resulting in lower lattice thermal conductivity [13]. Consequently, topological semimetals are regarded as potential high-performance thermoelectric materials.

Among topological semimetals, nodal-line semimetals [9] have attracted considerable interest due to their unique characteristics. These materials feature linearly dispersing bands that touch along continuous lines near the Fermi level [9,14], resulting in topologically protected one-dimensional (1D) loops in the Brillouin zone. Unlike other topological nodes, nodal-line semimetals possess intrinsic 1D loops or drumhead surface states, leading to a sharp and large density of states (DOSs) at the Fermi level. This attribute contributes to the presence of nonvanishing and large Seebeck coefficients [5], which are essential for thermoelectric applications. Several materials such as $CaTX(T = Ag,Cd, X = As,Ge,P)$ [15,16], $TlTaSe_2$ [17], $PbTaSe_2$ [18], $XO_2(X = Ir, Os, Ru)$ [19], and $ZrXY(X = Si,Ge, Y = S,Se,Te)$ [20–22] have been verified experimentally as nodal-line semimetals. Under the scalar relativistic approximation, CaAgAs(P) is an ideal nodal-line semimetal without any trivial bands around the Fermi level, and the introducing of SOC effect only turns on a small energy gap of less than 20 meV [15,23]. Of particular interest, CaAgP has been experimentally shown to possess good thermoelectric performance even without doping ($ZT = 0.32$ at 800 K) [24]. Consequently, $CaTX$ materials, including CaCdGe, provide an ideal platform for studying topological thermoelectricity.

CaCdGe, a sister compound of CaAgAs and CaAgP, shares a similar topological nodal-line structure but exhibits more complex fermiology [15]. Pressure, as an effective control

*wug@ihpc.a-star.edu.sg

†xpyang@hmfl.ac.cn

parameter, offers the means to systematically tune crystal structures and associated electronic states [25–27]. Understanding the pressure-induced variation of physical properties is crucial for tailoring materials for device applications. In CaCdGe, the nontrivial bands are topologically protected, and under the condition of unchanged space inversion and time reversal symmetries, external pressure can modulate the electron occupation of these bands and reshape the Fermi surface by renormalizing trivial bands. Consequently, new physics and phases emerge. In this study, we demonstrate that semimetal CaCdGe possesses an ultralow room temperature lattice thermal conductivity at 0 GPa (0.765 Wm^{-1}K^{-1}) and exhibits typical wide temperature range n-type thermoelectric behavior with ZT ranging from minimum 0.75 at 300 K to maximum 1.02 at 700 K in the $x(y)$ direction, and from minimum 0.23 at 300 K to maximum 0.65 at 1100 K in the z direction. Even under high pressures of up to 50 GPa, CaCdGe maintains its structural stability without undergoing any phase transitions, and its room temperature lattice thermal conductivity remains below 10 Wm^{-1}K^{-1}. Additionally, our investigation with spin-orbit coupling reveals a pressure-driven Lifshitz transition of the Fermi surface and a concurrent electronic phase transition around 40 GPa, transforming CaCdGe from a charge-compensated semimetal into a topological insulator. As the pressure increases, the in-plane $ZT_{\max}$ in high-temperature region is increased effectively, and reaches 1.2 at 1500 K and 50 GPa. Our findings underscore the remarkable thermoelectric potential of CaCdGe and related topological semimetallic materials, even under extreme conditions of high pressure and high temperature.

II. COMPUTATIONAL DETAILS

The high-pressure behavior was first explored by merging the evolutionary algorithm and *ab initio* total-energy calculations, as implemented in the USPEX [28,29]. Structures (population size: 20 structures) were produced randomly in the first generation. The subsequent generation is created from 60% of the lowest-enthalpy structures of the preceding generation. New structures are created by heredity (60%), permutation (10%), and lattice mutation (30%) operations. The best structure of each generation is also carried over to the next generation. The calculation stops when the best structure does not change for more than 20 generations. No structural phase transition is observed till 50 GPa (see Fig. S1 of Supplemental Material [30]), and the high-pressure phonon spectrum also does not exhibit imaginary frequencies or soft modes (see Fig. S2). Then we carried out electronic structure calculations by the projector augmented-wave (PAW) method and generalized gradient approximation (GGA) in the scheme of Perdew-Burke-Ernzerhof (PBE) exchange-correlation functional, as implemented in the Vienna *ab initio* simulation package (VASP) [31,32]. For an accurate band structure description, SOC effect and the modified Becke-Johnson (mBJ) [33] exchange-correlation potential were further introduced. The uniform plane wave cutoff energy was set to 520 eV. The k-point interval in the first Brillouin zone (BZ) was 0.02 Å^{-1}. The crystal structure was fully optimized until the interatomic force less than 10^{-3} eV/Å and total energy converged to 10^{-8} eV per unit cell.

The performance of thermoelectric materials is typically evaluated in terms of a dimensionless constant ZT, defined as $ZT = S^2 \sigma T / \kappa$, in which S, σ, T, and κ are the Seebeck coefficient, electrical conductivity, absolute temperature, and total thermal conductivity, respectively [34]. Thermal conductivity κ is the sum of electrical and lattice contributions, $\kappa = \kappa^e + \kappa^l$. To assess the electrical transport coefficients (S, σ/τ, κ^e/τ), we employ the BoltzTraP2 within the relaxation time (τ) approximation [35]. The second-order force constants and phonon dispersions are calculated using the $2 \times 2 \times 3$ supercell and the finite displacement method implemented in VASP and Phonopy [36], while the third-order (anharmonic) force constants and lattice thermal conductivity are determined using $2 \times 2 \times 2$ supercell and the PHONO3PY package [37]. Lattice thermal conductivity tensor is calculated by using the single mode relaxation time approximation (RTA) and linearized phonon Boltzmann equation. To ensure convergence in lattice thermal conductivity calculations, we employed a dense q mesh ($20 \times 20 \times 20$) and refrained from using a cutoff pair distance for reducing the number of supercells with displacements.

The calculations of thermoelectric transport coefficients in BoltzTraP2 utilize the rigid-band approximation (RBA), assuming that altering temperature or doping does not change the band structure. In the RBA, the carrier concentration (ρ) for a given temperature (T) and chemical potential (μ) can be determined from the density of states (n) through the charge neutrality condition: $\rho(\mu, T) = N - \int n(\varepsilon) f^{(0)}(\varepsilon; \mu, T) d\varepsilon$. In this equation, N is the nuclear charge, and $f^{(0)}$ is the Fermi distribution function, dependent on the chemical potential. The density of states is given by $n(\varepsilon) = \int \sum_b \delta(\varepsilon - \varepsilon_{b,\mathbf{k}}) \frac{d\mathbf{k}}{8\pi^3}$, where the subscript b runs over bands. This relationship allows us to establish the connection between carrier concentration and chemical potential, along with other thermoelectric properties.

III. RESULTS AND DISCUSSION

CaCdGe has a ZrNiAl-type hexagonal structure with space group P-$62m$ [38]. The crystal structure [see Fig. 1(a)] is composed of nine atoms (three Ca, three Cd, and three Ge) arranged in a network of corner- and edge-sharing CdGe$_4$ tetrahedra, with a mirror reflection plane located at the Ca plane intersecting two layers of CdGe$_4$ tetrahedra. Figures 1(b) and 1(c) show high symmetry k-point paths in the bulk hexagonal BZ of CaCdGe and its electronic band structure at 0 GPa, respectively. Without SOC included, two almost linear bands (thin black lines) cross just above the Fermi level along Γ-M and K-Γ paths, similar to that found in CaAgAs, indicating that CaCdGe has Dirac nodal-line features around the Fermi level. However, nodal-lines open a tiny gap (43 meV) due to strong SOC effect, mirror reflection symmetry, and inversion symmetry breaking [39], resulting in two hole pockets (blue band) around the Γ point. Besides nontrivial linear band dispersion, a trivial electronic pocket (red band) locates around the K-point. Consequently, CaCdGe exhibits charge-compensated semimetal behavior.

To gain direct insights into the evolution of CaCdGe's electronic properties under pressure, we calculated the electronic band structures at four representative pressure points (0, 20,
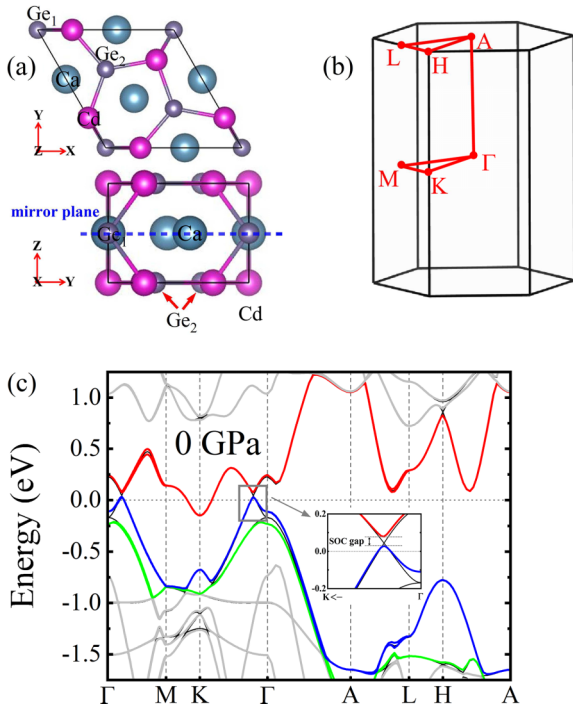
FIG. 1. (a) Schematic geometrical structures: top view and side view of CaCdGe. (b) The first Brillouin zone and high symmetry points. (c) GGA+mBJ band structures at 0 GPa with (thick line in color) and without (thin black line) SOC. The insect in panel (c) is the enlarged band structure around the Fermi level along K-Γ path.

40, 50 GPa). The results in Fig. 2 demonstrate that pressure induces band renormalization, causing the electronic pocket around the K-point to gradually vanish and the hole pockets along the Γ-M and K-Γ paths to become fully occupied at 40 GPa. This results in a Lifshitz transition of the Fermi surface and an electronic phase transition from a charge-compensated semimetal to a topological insulator with a reduced nodal-line gap of 20 meV. Notably, the electronic band structures exhibit significant conduction band convergence (CBC) [40],
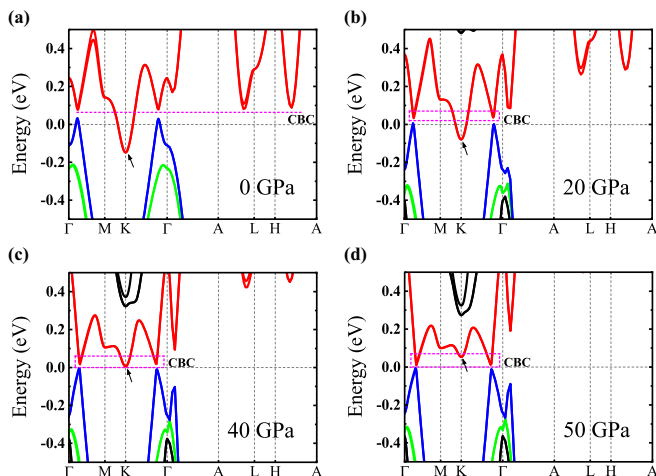

FIG. 2. The GGA+mBJ+SOC band structures of CaCdGe at 0, 20, 40, and 50 GPa.

as we can see in Fig. 2, which promotes high DOSs and high Seebeck coefficients. Furthermore, the asymmetry between the conduction and valence bands near the Fermi level enhances the Seebeck coefficient [12,13].

Understanding the electrical transport properties of materials under high-pressure conditions is essential for advancing their thermoelectric applications. The analysis of Fig. 3 reveals strong directional dependence of the electrical transport coefficients as functions of carrier concentrations (from 10^{19} to 10^{22} cm^{-3}), due to the anisotropy of the crystal structure. To gain further insights into the temperature dependence of these coefficients, we investigate their behavior at temperatures ranging from 300 to 1100 K. At ambient pressure (0 GPa), we observe that the peak values of the $|S|$, σ/τ, and $S^2\sigma/\tau$ for electron doping are consistently larger than those for hole doping along both the $x(y)$ and z directions. And the peak values of $|S|$ are comparable in magnitude to those of traditional semiconductor thermoelectric materials, which is attributed to the asymmetry of energy bands around the Fermi level and the CBC effect, as mentioned earlier.

At 0 GPa and 300 K, we find that the electrical conductivity σ/τ remains very small in the low carrier concentration region but rapidly increases once doping exceeds 10^{21} cm^{-3}. The electrical thermal conductivity κ^e/τ follows a similar trend to the electrical conductivity σ/τ due to the Wiedemann-Franz law, where $\kappa^e = L\sigma T$ and L is the Lorenz number. As the temperature increases, κ^e/τ gradually increases while σ/τ remains stable, in accordance with the Wiedemann-Franz law. Additionally, both the electrical and lattice thermal conductivities (to be discussed in Fig. 4 and Fig. S2) in the z direction are larger than those in the $x(y)$ direction, resulting in smaller ZT values in the z direction (as shown in Fig. 7), even though the power factor $S^2\sigma/\tau$ in the z direction is relatively larger at temperatures ranging from 900 to 1100 K.

Under increasing pressure, the $|S|$ and σ/τ experience renormalization due to the pressure response of energy bands around the Fermi level. In the fatband structures (see Figs. S3 and S4), we observe that two trivial conduction band valleys along the A-L-H-A path are mainly contributed by p orbitals of Cd and Ge atoms. Increasing pressure causes these valleys to shift toward higher energies, resulting in weakened peak values of $|S|$ for electron doping in the $x(y)$ direction at 300 K. For hole doping at 40 and 50 GPa, we observe sign changes in the Seebeck coefficients at low carrier concentrations due to the occupation of hole pockets along the Γ-M and K-Γ directions. As the hole doping concentration exceeds 10^{21} cm^{-3}, pressure leads to larger σ/τ and κ^e/τ, particularly after the phase transition at 40 and 50 GPa. Overall, CaCdGe remains an n-type thermoelectric material under high pressure, with the peak value of $S^2\sigma/\tau$ in the $x(y)$ direction exhibiting an increase with pressure, while the change in the z direction is reversed. Furthermore, since only the topologically protected nontrivial energy bands cross the Fermi level after the phase transition [see Figs. 2(c) and 2(d)], the electrical transport coefficients become insensitive to the applied pressure after 40 GPa, as we can see in Fig. 3, and the system exhibits unconventional pressure response behavior.

The efficiency of thermoelectric materials is not only determined by their electrical transport properties but also by their lattice thermal conductivity, which is closely related to
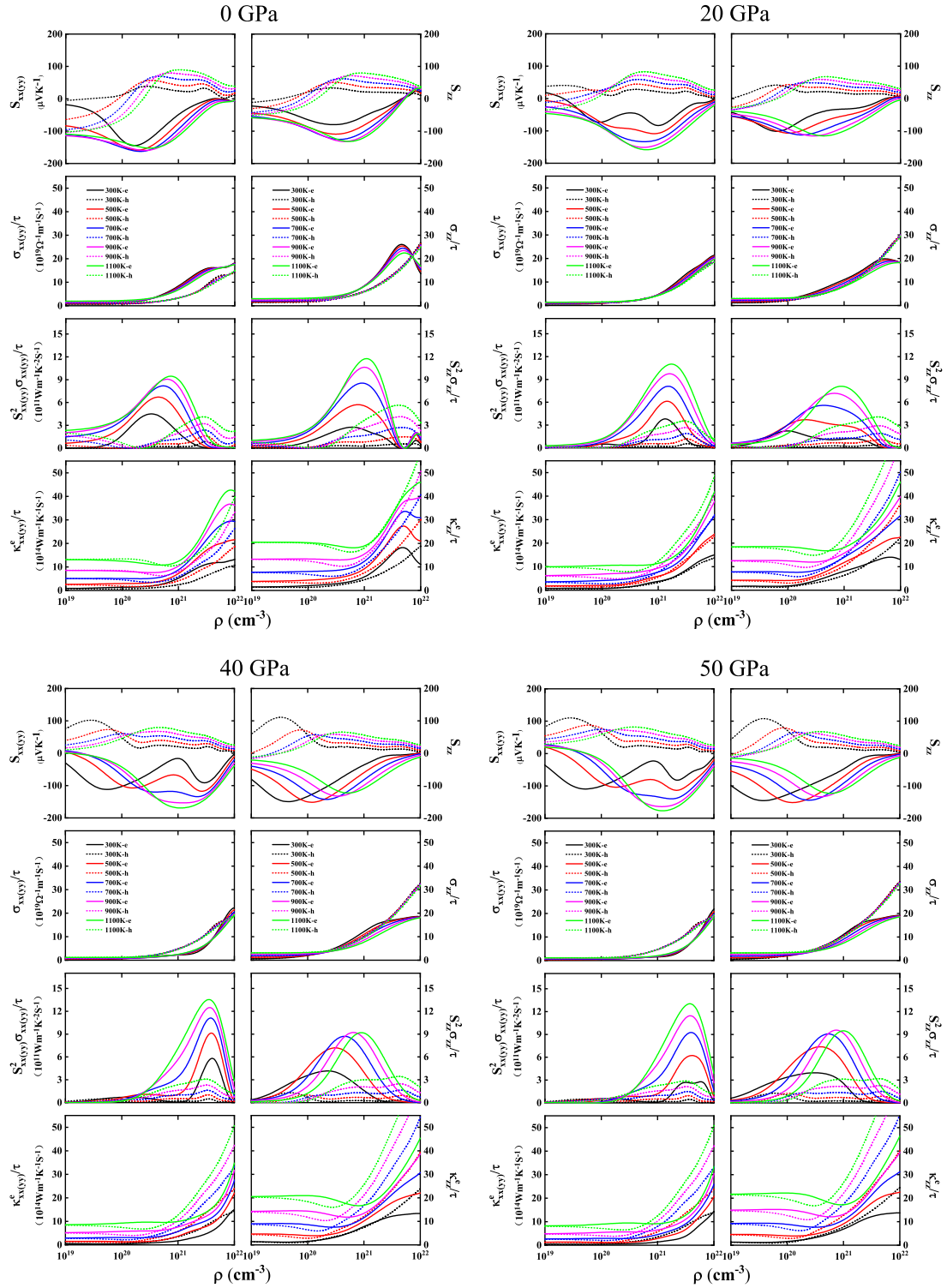
FIG. 3. Seebeck coefficient S, electrical conductivity σ/τ, power factor $S^2\sigma/\tau$, and electrical thermal conductivity κ^e/τ of CaCdGe at 0, 20, 40, and 50 GPa in the $x(y)$ and z directions as functions of the electron doping (solid lines) and hole doping (dash lines) concentrations.

the phonon dispersion. In Fig. 4(a), we present the phonon dispersion of CaCdGe at 0 GPa. Notably, we observe a significant mixing of low-frequency acoustic phonons and optical phonons, particularly the longitudinal acoustic (LA) mode. This behavior suggests a strong acoustic-optical coupling in CaCdGe due to the close up of the acoustic-optic frequency gap. Typically, heat transport in materials is primarily

contributed by acoustic phonons. Based on kinetic theory, the lattice thermal conductivity κ^l can be determined using the equation $\kappa^l = \frac{1}{3}C_V v_g^2 \tau'$. Here, C_V represents the heat capacity, v_g corresponds to the phonon group velocity, and τ' signifies the phonon lifetime. In the case of CaCdGe, the pronounced acoustic-optical coupling leads to an increase in scattering rates caused by three-phonon processes (acoustic + acoustic
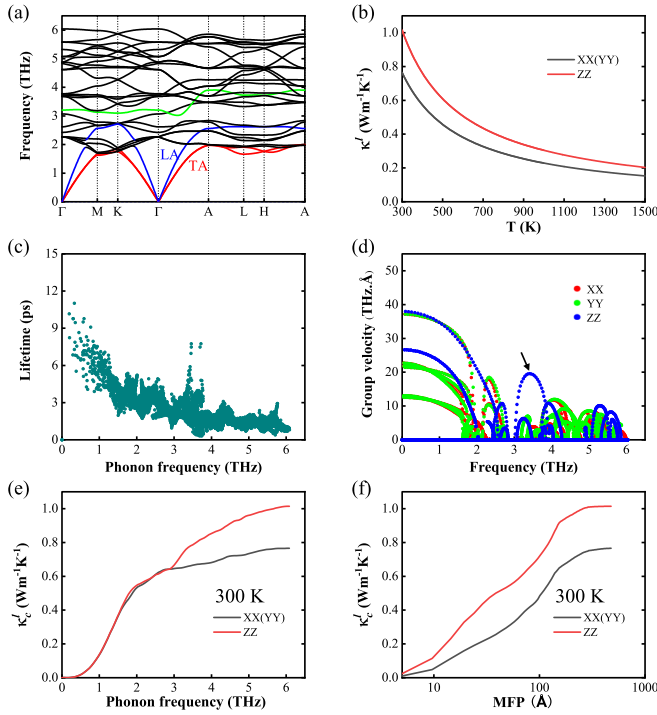
FIG. 4. Lattice dynamic properties of CaCdGe at 0 GPa. (a) Phonon band structure, (b) lattice thermal conductivity κ^l as a function of the temperature, (c) lifetime as a function of the frequency, (d) phonon group velocity as a function of the frequency, (e) cumulative lattice thermal conductivity κ_c^l as a function of the frequency, and (f) cumulative lattice thermal conductivity κ_c^l as a function of the phonon mean free path.

FIG. 5. Lattice thermal conductivity κ^l under different pressure as a function of the temperature.

$\rightarrow$ optical, acoustic + optical $\rightarrow$ optical). Consequently, the phonon lifetime is reduced, as illustrated in Fig. 4(c), resulting in the suppression of lattice thermal conductivity κ^l. Our calculations reveal that CaCdGe exhibits an ultralow lattice thermal conductivity of 0.765 and 1.014 Wm^{-1}K^{-1} in the $x(y)$ and z directions, respectively, at room temperature, as depicted in Fig. 4(b). These findings underscore the significant influence of the acoustic-optical coupling on the thermal properties of CaCdGe.

We analyze the changes in cumulative lattice thermal conductivity κ_c^l as a function of phonon frequency and phonon mean free path (MFP) at 300 K, as summarized in Figs. 4(e) and 4(f). Figure 4(e) demonstrates that below 3 THz, the κ_c^l is similar in both directions, but exhibits a strong directional dependence above this frequency range. This discrepancy arises from the anisotropic group velocities observed above 3 THz, as depicted in Fig. 4(d). Particularly, a distinct distribution of high group velocities along the z direction between 3 and 4 THz is observed, and their corresponding phonon dispersions are represented by a green line in Fig. 4(a). Interestingly, the phonon shows minimal dispersion in the xy plane, while the phonon bandwidth along the Γ-A path can reach 1 THz. Furthermore, Fig. 4(f) illustrates that the lattice thermal conductivity of CaCdGe saturates in both directions once the phonon MFP exceeds 50 nm. This indicates that the MFP in CaCdGe is shorter than, or comparable to, the size of the crystalline grain typically observed in crystalline materials.
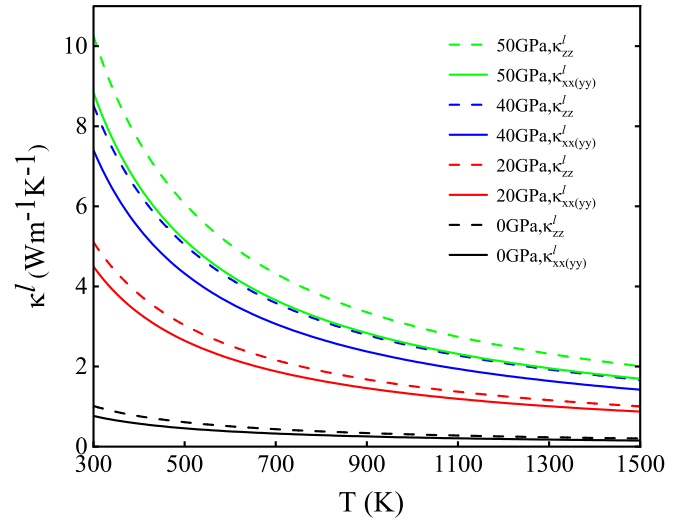
Consequently, we propose that structure engineering, such as nanostructuring or polycrystalline structures, could be an effective experimental approach to reducing the thermal conductivity in CaCdGe.

Figure 5 showcases the relationship between lattice thermal conductivity κ^l and temperature under various pressures. We observe a monotonous decrease in κ^l with increasing temperature in both directions, consistent with the expected T^{-1} temperature dependence in regimes dominated by Umklapp scattering. Additionally, pressure leads to the hardening of phonon modes, as we can see in Fig. 6 and Fig. S2. Above 20 GPa, the transverse acoustic (TA) mode no longer intersects with low-frequency optical modes, resulting in a decrease in three-phonon scattering rates and an increase in lattice thermal conductivity. This observation is supported by the increasing group velocity and phonon lifetime with pressure (see Fig. 6 and Fig. S2). By analyzing the phonon band structures under different pressures in Fig. S2, we observe that the hardening amplitude of optical modes and the LA mode surpasses that of the TA mode. The optical modes and LA mode consistently intersect, enabling κ^l to remain below 10 Wm^{-1}K^{-1} even at high pressures of 50 GPa, which is lower than the values observed in most 2D thermoelectric materials such as WSe$_2$ (34 Wm^{-1}K^{-1}) [41], MoSe$_2$ (62 Wm^{-1}K^{-1}) [41], and MoS$_2$ (123 Wm^{-1}K^{-1}) [42]. It should be noted that experimental lattice thermal conductivity under high pressure may exhibit a more modest increase than our predictions due to enhanced scattering at grain boundaries resulting from reduced grain size under high pressure.

To obtain the precise ZT value, we calculated the relaxation time (τ_e and τ_h) using the formula $\tau = \frac{m^*\mu}{e}$, where e is the elementary charge, m^* is the effective mass, and μ is the mobility. Experimental data for effective mass and temperature-dependent mobilities (μ_e and μ_h) were obtained from Emmanouilidou *et al.* [15]. The effective mass of electrons in CaCdGe was reported as 0.23 m_e, and the mobilities range from 0.7(0.3) m^{2}V^{-1}s^{-1} at 2 K to 0.159(0.105) m^{2}V^{-1}s^{-1} at 150 K for electrons (holes),
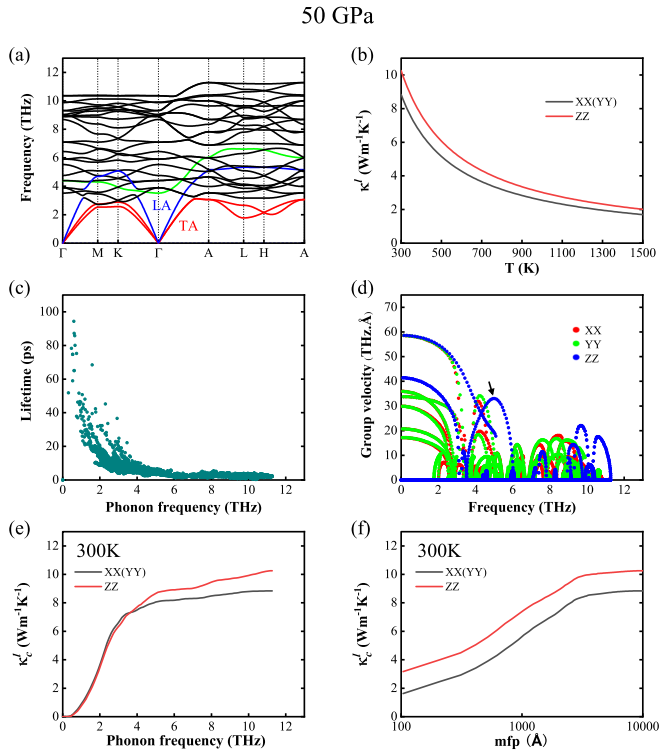
FIG. 6. Lattice dynamic properties of CaCdGe at 50 GPa. (a) Phonon band structure, (b) lattice thermal conductivity κ^l as a function of the temperature, (c) lifetime as a function of the frequency, (d) phonon group velocity as a function of the frequency, (e) cumulative lattice thermal conductivity κ_c^l as a function of the frequency, and (f) cumulative lattice thermal conductivity κ_c^l as a function of the phonon mean free path.

respectively. For simplicity, we assumed that the effective mass of holes (m_h^*) is equal to that of electrons (m_e^*) since experimental measurements for m_h^* in CaCdGe are unavailable. To assess the potential discrepancy between m_e^* and m_h^*, we calculated the effective mass of energy bands at the Fermi level. Overall, we observed that m_h^* is of the same order of magnitude as m_e^*, with a minor difference ($0.01m_e$) between them. Given that CaCdGe is an *n*-type thermoelectric material, this simplified approximation of $m_h^* = m_e^*$ remains reasonable and does not qualitatively impact our calculation results. Furthermore, we observed an inverse relationship between mobilities and temperature, i.e., $\mu \propto T^{-1}$, in the temperature range of 50 K to 150 K. Based on this trend, we fit the relaxation time τ_e and τ_h values above 150 K, as listed in Table S1.

We utilize various calculation results, including τ, S, σ/τ, κ^e/τ, and κ^l, to determine the *ZT* as functions of carrier concentrations at different temperatures and pressures in Fig. 7. Our findings demonstrate that CaCdGe holds promise as a wide-temperature-range *n*-type thermoelectric material at 0 GPa. The low lattice thermal conductivity renders the *ZT* values of CaCdGe relatively insensitive to the relaxation time τ, particularly at high temperatures. At 0 GPa, the ZT_{max} values for electron-doped CaCdGe are 1.02 at 700 K and 0.65 at 1100 K along the $x(y)$ and z directions, respectively. The relatively higher electrical and lattice thermal conductivities
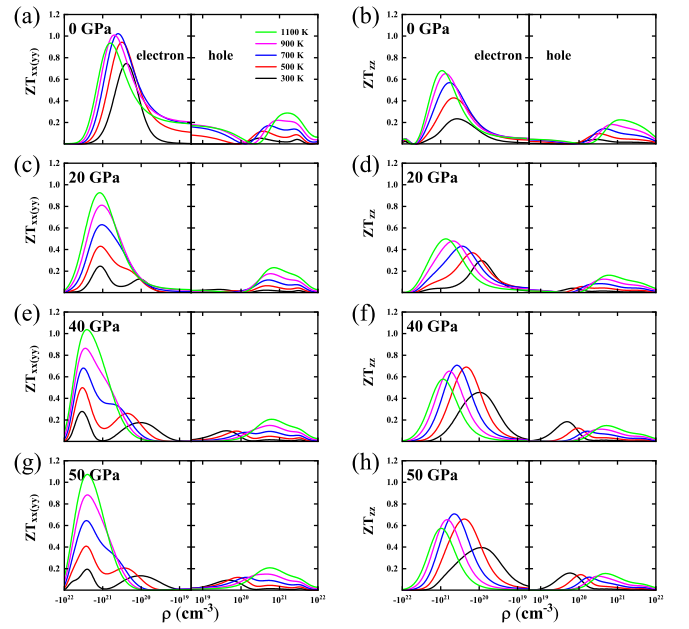

FIG. 7. *ZT* values of CaCdGe in the $x(y)$ and z direction as functions of the carrier (electron and hole) concentrations from 300 to 1100 K.

in the z direction contribute to the lower *ZT* value in that direction. Under electron doping, applied pressure causes the in-plane *ZT* peak positions to be closely aligned across all temperatures and shift to higher doping concentrations. Additionally, a new short *ZT* peak emerges at low concentration and temperature. The out-of-plane *ZT* peak positions gradually shift to lower concentrations with decreasing temperature.

The evolution of ZT_{max} with respect to temperature and pressure is illustrated in Fig. 8. Under electron doping, we observe two critical temperature points (T_1 and T_2) in both in-plane and out-of-plane directions. T_1 and T_2 represent critical temperatures before and after the phase transition, respectively. For temperatures lower than T_1(T_2), pressure causes the
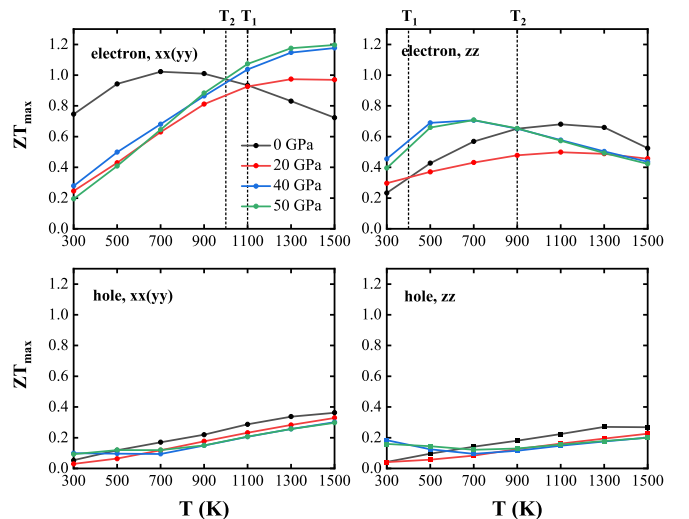

FIG. 8. ZT_{max} of CaCdGe for electron and hole doping in the $x(y)$ and z direction as functions of temperature and pressure.

in-plane ZT_{max} to be smaller than the value at 0 GPa. Conversely, for temperatures higher than $T_1(T_2)$, pressure leads to an increased in-plane ZT_{max} compared to the value at 0 GPa, particularly reaching 1.2 at 50 GPa and 1500 K after the phase transition. The change in the out-of-plane ZT_{max} value caused by pressure exhibits an opposite trend, and the out-of-plane ZT_{max} can reach 0.7 at 50 GPa and 500 K after the phase transition. The effect of pressure on thermoelectric properties under hole doping is relatively weak. Only at concentrations smaller than 10^{20} cm^{-3} in Fig. 7 and temperatures below 500 K in Fig. 8, do we observe slight improvements after the phase transition in both in-plane and out-of-plane ZT and ZT_{max} values.

IV. CONCLUSIONS

By employing a first-principles method and semiclassical Boltzmann transport theory, we have investigated the electronic structures, lattice dynamics, thermoelectric properties of semimetal CaCdGe, and their response to pressure. Our calculations revealed that CaCdGe undergoes a pressure-driven Lifshitz transition of the Fermi surface around 40 GPa, accompanied by an electronic phase transition from a charge-compensated semimetal to a topological insulator with a small energy gap. Under ambient pressure, CaCdGe exhibits ultralow lattice thermal conductivity at room temperature

$(0.765$ Wm^{-1}K$^{-1})$ and demonstrates typical behavior of a wide temperature range n-type thermoelectric material, with the ZT ranging from 0.75 to 1.02 in the $x(y)$ direction and from 0.23 to 0.65 in the z direction across various temperatures. Despite increasing with pressure, the lattice thermal conductance κ^l remains below 10 Wm^{-1}K^{-1} even at high pressures 50 GPa, suggesting its potential for thermoelectric applications in extreme conditions. Furthermore, the electrical transport coefficients and ZT present unconventional pressure response, mainly manifested in their insensitivity to high pressure after topological electronic phase transition. Even at high pressure of 50 GPa, in-plane (out-of-plane) ZT_{max} can reach 1.2 (0.7) at 1500 K (500 K). Our findings highlight the promising prospects of CaCdGe and related topological materials for thermoelectric applications under ambient and extreme pressure and temperature conditions.

[1] F. Han, N. Andrejevic, T. Nguyen, V. Kozii, Q. T. Nguyen, T. Hogan, Z. Ding, R. Pablo-Pedro, S. Parjan, B. Skinner, A. Alatas, E. Alp, S. Chi, J. Fernandez-Baca, S. Huang, L. Fu, and M. Li, Quantized thermoelectric Hall effect induces giant power factor in a topological semimetal, Nat. Commun. **11**, 6167 (2020).

[2] B. Skinner and L. Fu, Large, nonsaturating thermopower in a quantizing magnetic field, Sci. Adv. **4**, eaat2621 (2018).

[3] C. Fu, Y. Sun, and C. Felser, Topological thermoelectrics, APL Mater. **8**, 040913 (2020).

[4] C. Rudderham and J. Maassen, *Ab initio* thermoelectric calculations of ring-shaped bands in two-dimensional Bi$_2$Te$_3$, Bi$_2$Se$_3$, and Sb$_2$Te$_3$: Comparison of scattering approximations, Phys. Rev. B **103**, 165406 (2021).

[5] M. Hosoi, I. Tateishi, H. Matsuura, and M. Ogata, Thin films of topological nodal line semimetals as a candidate for efficient thermoelectric converters, Phys. Rev. B **105**, 085406 (2022).

[6] M. Markov, X. Hu, H. C. Liu, N. Liu, S. J. Poon, K. Esfarjani, and M. Zebarjadi, Semi-metals as potential thermoelectric materials, Sci. Rep. **8**, 9876 (2018).

[7] S. M. Young, S. Zaheer, J. C. Y. Teo, C. L. Kane, E. J. Mele, and A. M. Rappe, Dirac semimetal in three dimensions, Phys. Rev. Lett. **108**, 140405 (2012).

[8] A. A. Soluyanov, D. Gresch, Z. Wang, Q. Wu, M. Troyer, X. Dai, and B. A. Bernevig, Type-II Weyl Semimetals, Nature (London) **527**, 495 (2015).

[9] A. A. Burkov, M. D. Hook, and L. Balents, Topological nodal semimetals, Phys. Rev. B **84**, 235126 (2011).

[10] H. Weng, Y. Liang, Q. Xu, R. Yu, Z. Fang, X. Dai, and Y. Kawazoe, Topological node-line semimetal in threedimensional graphene networks, Phys. Rev. B **92**, 045108 (2015).

[11] X. Wan, A. M. Turner, A. Vishwanath, and S. Y. Savrasov, Topological semimetal and Fermi-arc surface states in the electronic structure of pyrochlore iridates, Phys. Rev. B **83**, 205101 (2011).

[12] S. Barati and S. H. Abedinpour, Thermoelectric response of nodal-line semimetals: Probing the Fermi surface topology, Phys. Rev. B **102**, 125139 (2020).

[13] M. Markov, S. E. Rezaei, S. N. Sadeghi, K. Esfarjani, and M. Zebarjadi, Thermoelectric properties of semimetals, Phys. Rev. Mater. **3**, 095401 (2019).

[14] C. Fang, Y. Chen, H. Y. Kee, and L. Fu, Topological nodal line semimetals with and without spin-orbital coupling, Phys. Rev. B **92**, 081201(R) (2015).

[15] E. Emmanouilidou, B. Shen, X. Deng, T. R. Chang, A. Shi, G. Kotliar, S.-Y. Xu, and N. Ni, Magnetotransport properties of the single-crystalline nodal-line semimetal candidates CaTX ($T =$ Ag, Cd; $X =$ As, Ge), Phys. Rev. B **95**, 245113 (2017).

[16] N. Xu, Y. T. Qian, Q. S. Wu, G. Autès, C. E. Matt, B. Q. Lv, M. Y. Yao, V. N. Strocov, E. Pomjakushina, K. Conder, N. C. Plumb, M. Radovic, O. V. Yazyev, T. Qian, H. Ding, J. Mesot, and M. Shi, Trivial topological phase of CaAgP and the topological nodal-line transition in CaAg(P$_{1-x}$As$_x$), Phys. Rev. B **97**, 161111(R) (2018).

[17] G. Bian, T. R. Chang, H. Zheng, S. Velury, S. Y. Xu, T. Neupert, C.-K. Chiu, S.-M. Huang, D. S. Sanchez, I. Belopolski, N. Alidoust, P.-J. Chen, G. Chang, A. Bansil, H.-T. Jeng, H. Lin, and M. Z. Hasan, Drumhead surface states and topological nodal-line fermions in TlTaSe$_2$, Phys. Rev. B **93**, 121113(R) (2016).

[18] G. Bian, T.-R. Chang, R. Sankar, S.-Y. Xu, H. Zheng, T. Neupert, C.-K. Chiu, S.-M. Huang, G. Chang, I. Belopolski, D. S. Sanchez, M. Neupane, N. Alidoust, C. Liu, B. Wang, C.-C.

Lee, H. T. Jeng, C. Zhang, Z. Yuan, S. Jia *et al.*, Topological nodal-line fermions in spin-orbit metal PbTaSe$_2$, Nat. Commun. **7**, 10556 (2016).

[19] Y. Sun, Y. Zhang, C. X. Liu, C. Felser, and B. Yan, Dirac nodal lines and induced spin Hall effect in metallic rutile oxides, Phys. Rev. B **95**, 235104 (2017).

[20] M. Neupane, I. Belopolski, M. M. Hosen, D. S. Sanchez, R. Sankar, M. Szlawska, S.-Y. Xu, K. Dimitri, N. Dhakal, P. Maldonado, P. M. Oppeneer, D. Kaczorowski, F. Chou, M. Z. Hasan, and T. Durakiewicz, Observation of topological nodal fermion semimetal phase in ZrSiS, Phys. Rev. B **93**, 201104(R) (2016).

[21] A. Topp, J. M. Lippmann, A. Varykhalov, V. Duppel, B. V. Lotsch, C. R. Ast, and L. M. Schoop, Non-symmorphic band degeneracy at the Fermi level in ZrSiTe, New J. Phys. **18**, 125014 (2016).

[22] Salmankurt Bahadir and S. Duman, First-principles study of structural, mechanical, lattice dynamical and thermal properties of nodal-line semimetals ZrXY (X= Si, Ge; Y= S, Se), Philos. Mag. **97**, 175 (2017).

[23] X. B. Wang, X. M. Ma, E. Emmanouilidou, B. Shen, C.-H. Hsu, C.-S. Zhou, Y. Zuo, R.-R. Song, S.-Y. Xu, G. Wang, L. Huang, N. Ni, and C. Liu, Topological surface electronic states in candidate nodal-line semimetal CaAgAs, Phys. Rev. B **96**, 161112(R) (2017).

[24] R. J. Quinn and J. W. G. Bos, Promising thermoelectric performance in CaAgP with intrinsic Ag vacancies, Appl. Phys. Lett. **120**, 073903 (2022).

[25] L. C. Chen, P. Q. Chen, W. J. Li, Q. Zhang, V. V. Struzhkin, A. F. Goncharov, Z. Ren, and X. J. Chen, Enhancement of thermoelectric performance across the topological phase transition in dense lead selenide, Nat. Mater. **18**, 1321 (2019).

[26] N. M. Alsaleh, E. Shoko, M. Arsalan, and U. Schwingenschlögl, Thermoelectric materials under pressure, Phys. Status Solidi RRL **12**, 1800083 (2018).

[27] Y. Zhou, Z. Y. Dong, W. P. Hsieh, A. F. Goncharov, and X. J. Chen, Thermal conductivity of materials under pressure, Nat. Rev. Phys. **4**, 319 (2022).

[28] A. R. Oganov and C. W. Glass, Crystal structure prediction using *ab initio* evolutionary techniques: principles and applications, J. Chem. Phys. **124**, 244704 (2006).

[29] A. O. Lyakhov, A. R. Oganov, H. T. Stokes, and Q. Zhu, New developments in evolutionary structure prediction algorithm USPEX, Comput. Phys. Commun. **184**, 1172 (2013).

[30] See Supplemental Material at http://link.aps.org/supplemental/10.1103/PhysRevB.109.035166 for detailed information on temperature dependence of relaxation time and pressure dependence of lattice dynamics and orbital-resolved electronic structures.

[31] G. Kresse and J. Furthmüller, Efficiency of *ab initio* total energy calculations for metals and semiconductors using a plane-wave basis set, Comput. Mater. Sci. **6**, 15 (1996).

[32] G. Kresse and J. Furthmüller, Efficient iterative schemes for *ab initio* total-energy calculations using a plane-wave basis set, Phys. Rev. B **54**, 11169 (1996).

[33] F. Tran and P. Blaha, Accurate band gaps of semiconductors and insulators with a semilocal exchange-correlation potential, Phys. Rev. Lett. **102**, 226401 (2009).

[34] D. M. Rowe, *Thermoelectrics Handbook: Macro to Nano* (CRC Press, Boca Raton, 2018).

[35] G. K. Madsen, J. Carrete, and M. J. Verstraete, BoltzTraP2, a program for interpolating band structures and calculating semi-classical transport coefficients, Comput. Phys. Commun. **231**, 140 (2018).

[36] A. Togo and I. Tanaka, First principles phonon calculations in materials science, Scr. Mater. **108**, 1 (2015).

[37] A. Togo, First-principles phonon calculations with phonopy and phono3py, J. Phys. Soc. Jpn. **92**, 012001 (2023).

[38] A. Iandelli, The structure of some ternary phases of calcium, Revue de chimie minérale **24**, 28 (1987).

[39] S. Y. Yang, H. Yang, E. Derunova, S. S. Parkin, B. Yan, and M. N. Ali, Symmetry demanded topological nodal-line materials, Adv. Phys.: X **3**, 1414631 (2018).

[40] Y. Pei, X. Shi, A. LaLonde, H. Wang, L. Chen, and G. J. Snyder, Convergence of electronic bands for high performance bulk thermoelectrics, Nature (London) **473**, 66 (2011).

[41] S. Kumar and U. Schwingenschlogl, Thermoelectric response of bulk and monolayer MoSe$_2$ and WSe$_2$, Chem. Mater. **27**, 1278 (2015).

[42] Y. Zhao, Z. Dai, C. Zhang, C. Lian, S. Zeng, G. Li, S. Meng, and J. Ni, Intrinsic electronic transport and thermoelectric power factor in *n*-type doped monolayer MoS$_2$, New J. Phys. **20**, 043009 (2018).